ISSN 1027-4510, Journal of Surface Investigation: X-ray, Synchrotron and Neutron Techniques, 2023, Vol. 17, No. 6, pp. 1287–1294. © Pleiades Publishing, Ltd., 2023.

On the Formation and Investigation of Multilayer Films of a High-Entropy Alloy Obtained by the Ion-Plasma Method in a Nitrogen Environment

Yu. H. Ahmadeev[a, *], Yu. F. Ivanov[a], N. N. Koval[a], V. V. Shugurov[a], E. A. Petrikova[a], O. V. Krysina[a], N. A. Prokopenko[a, **], I. I. Azhazha[a], and A. N. Shmakov[b, c]

[a] *Institute of High Current Electronics, Siberian Branch, Russian Academy of Sciences, Tomsk, 634055 Russia*

[b] *Budker Institute of Nuclear Physics, Siberian Branch, Russian Academy of Sciences, Novosibirsk, 630090 Russia*

[c] *Federal Research Centre "SKIF," Boreskov Institute of Catalysis, Siberian Branch, Russian Academy of Sciences, Novosibirsk, 630090 Russia*

**e-mail: ahmadeev@opee.hcei.tsc.ru*

***e-mail: prokopenko@opee.hcei.tsc.ru*

Received November 17, 2022; revised January 19, 2023; accepted January 19, 2023

Abstract—A developed vacuum-arc plasma-assisted method is applied to produce films of a high-entropy alloy from a multicomponent gas-metal plasma generated by the simultaneous independent evaporation of selected metal cathodes. New modes are revealed to allow the deposition of thin films of a high-entropy alloy, AlTiCrNbMo–N, with a nearly equiatom composition. The films are a multilayer nanocrystalline material with a body-centered cubic lattice, the parameter of which specifically depends on the concentration of elements in the alloy. The synchrotron-radiation technique demonstrates that films of the high-entropy alloy AlTiCrNbMo–N are stable when heated in air to temperatures not exceeding 620°C.

Keywords: high-entropy alloys, cermet films, vacuum-arc plasma-assisted method, sputtering, phase composition, structure, microhardness, wear resistance

DOI: 10.1134/S1027451023060034

INTRODUCTION

In recent years, specialists in physical materials science have paid special attention to high-entropy alloys, which were first studied in [1–3]. They are based on several (at least five) elements with a concentration of 5–35 at % of each element. Reviews [4–7] concluded that due to the unique mechanical and physical–chemical properties (corrosion resistance, high thermal stability, wear resistance, increased strength and ductility), the fields of application of high-entropy alloys can be quite extensive.

The next step, expanding the prospect of using materials with high entropy, was the creation of nitride coatings based on them [8]. As rightly noted in [9], nitride coatings based on high-entropy alloys are metal-like compounds in which metallic bonds between metal atoms coexist with ion-covalent bonds between metal and nonmetal atoms; for this reason, they cannot be attributed to a special family of high-entropy alloys, as suggested in [5]. The microhardness of nitride coatings based on such alloys is their most frequently controlled characteristic. It essentially depends on such factors as elemental composition, crystallite size, and method of coating formation [4]. For example, nitride coatings obtained from high-entropy Ti–V–Zr–Nb–Hf alloys at a nitrogen pressure of 0.27 Pa showed the highest hardness among vacuum-arc coatings [10]. In the case of the [111] coating texture, an increase in the voltage at the substrate from –50 to –100 V increases the coating hardness from 59 to 64 GPa, while the appearance of a biaxial texture with the [111] and [110] axes at –200 V leads to the highest hardness, 70 GPa. The crystallite size in this case is 57 nm.

Having high hardness, high-entropy alloys and coatings based on them are relatively brittle materials [11–16]. One of the promising ways to improve their plastic properties without loss of strength is material nanostructuring [17, 18]. The methods of synchrotron and neutron research, developed in recent years and complementing X-ray structural and X-ray phase analysis (XRD), have been successfully employed to reveal and refine the phase composition and parameters of the crystalline structure, determine the atomic arrangement in the obtained high-entropy alloys and their nitrides, diagnose the stress fields formed in the films, and track the in situ structural changes of the material at elevated and high temperatures [19–22].

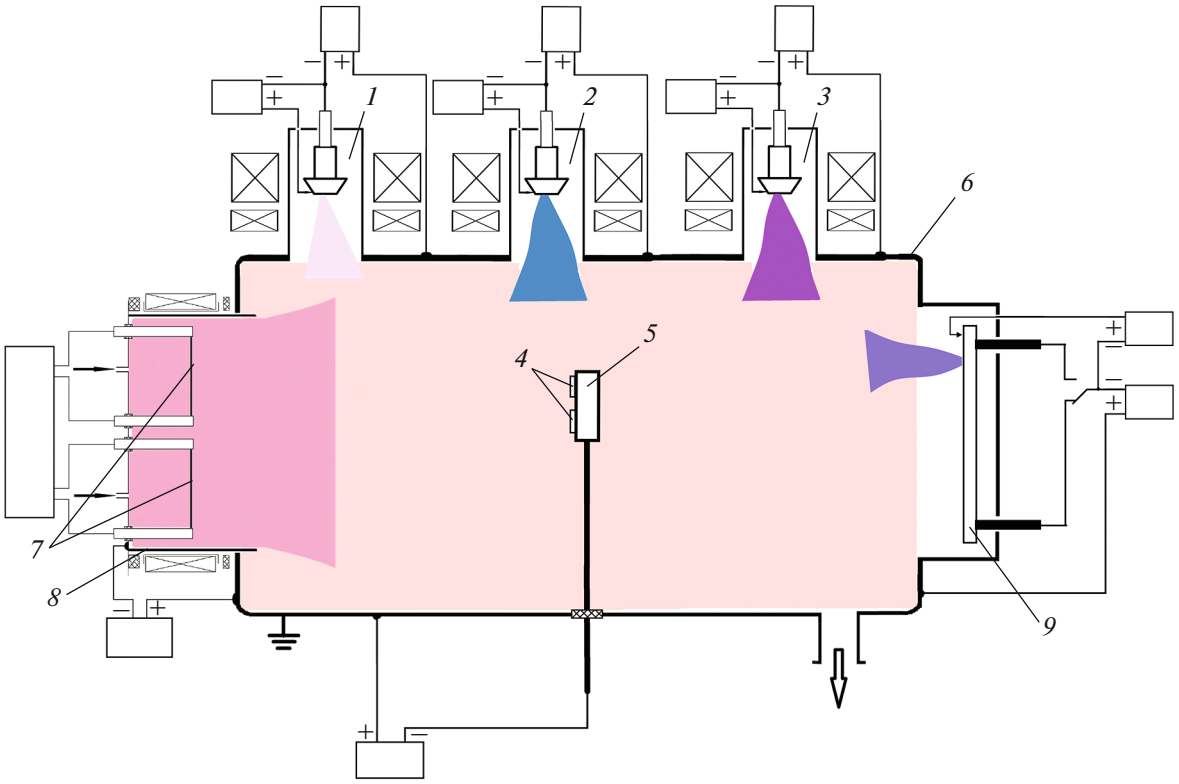

Fig. 1. Experimental setup for the deposition of high-entropy-alloy films: (*1*) DI100 arc evaporator with a Mo cathode, (*2*) DI80 arc evaporator with a Nb cathode, (*3*) DI100 arc evaporator with a Ti–Al cathode, (*4*) samples, (*5*) equipment, (*6*) vacuum chamber, (*7*) heated cathodes; (*8*) PINK-P gas-plasma generator, and (*9*) DP400 arc evaporator with a Cr cathode.

The study develops a method and reveals the formation regularities, structure, and properties of multilayer films of high-entropy AlTiCrNbMo–N alloys formed on the surface of a substrate by a vacuum-arc plasma-assisted deposition.

EXPERIMENTAL

Films of the high-entropy alloy NbMoCrTiAl–N with a thickness of 3–5 μm were formed by vacuum-arc plasma-assisted deposition on substrates made of commercially pure titanium VT1-0, VK8 hard alloy, and tungsten, using the QUINTA installation, the design and operation of which are described in [23, 24]. Films deposited on commercially pure titanium VT1-0 substrates were used to study the structure by scanning electron microscopy (SEM) and transmission electron microscopy (TEM). Films deposited on VK8 hard-alloy substrates were used for mechanical (determination of microhardness) and tribological (determination of the wear parameter and friction coefficient) tests, as well as for studying the phase composition by XRD. Films deposited on tungsten substrates were used to analyze the structure and heat resistance by synchrotron radiation (SR) diffraction. The QUINTA installation is part of the UNIQUUM complex of unique electrophysical installations, which is included in the list of unique scientific installations of the Russian Federation (http://ckprf.ru/usu/434216/) and the list of infrastructure registered in the Information and Analytical System of the Russian Science Foundation (https://grant.rscf.ru/site/user/browse_infra). The films were deposited using chromium, molybdenum, and niobium cathodes, as well as a 50% Ti–50% Al composite cathode. The experimental procedures to form high-entropy-alloy films are schematically shown in Fig. 1. Vacuum-arc plasma-assisted deposition has several advantages, including ecologically clean processes, automated cleaning of the substrate surfaces before coating, ion-plasma deposition, and the formation of films with a specific elemental composition. The process also allows for the stage-by-stage formation of cermet and ceramic films and coatings with precise control over the composition and thickness of the deposited layers.

We studied the deposition rate of individual coating components and the parameters of the generated plasma with the independent and joint operation of plasma sources. In experiments to measure the growth rate of coatings upon deposition, the average discharge current was selected as the operating discharge current of the electric-arc evaporator in the range from the minimum current during stable operation of the electric-arc evaporator to the maximum current provided

by the power source. The thickness of films and coatings was measured by the standardized Calotest method using a Calotest CAT-S-0000 instrument according to the geometric parameters of a spherical section. The metal film growth rate V_{dep} depends not only on the arc-discharge current I_d but also on the sputtered cathode material (Table 1).

The azimuthal distribution of the ion-current density of a gas plasma generator based on a non-self-sustained arc discharge with a termionic and hollow PINK-P cathode is shown in Fig. 2. The experiments were carried out at a pressure of the working-gas mixture of 0.3 Pa. We opted for two gas media: pure argon (Fig. 2a) and a mixture of argon and nitrogen in equal proportions (Fig. 2b). The collector was located on a satellite rotating orbitally around the axis of the manipulator of the vacuum chamber and passed from 17 cm to the outlet aperture of the plasma generator at the closest point to 55 cm from the outlet aperture at the farthest point.

The results of measuring the azimuthal distribution of the ion-current density of the gas-plasma generator suggested that at different discharge currents, the ion-current density varies from 0.7 to 15 mA/cm^2 for a discharge in an argon atmosphere and from 0.8 to 12.4 mA/cm^2 for a discharge in an argon–nitrogen mixture of equal proportions.

In experiments on the analysis of the uniformity of the azimuthal distribution of the ion-current density, we selected the operating mode of the plasma generators so that, considering the deposition rate of each cathode, the percentage mass ratio of the elements of the high-entropy-alloy film was observed. The following parameters were set: $I_{AlTi} = 170$, $I_{Cr} = 160$, $I_{Mo} = 110$, $I_{Nb} = 120$, and $I_{PINK\text{-}P} = 50$ A. The experiments were carried out at a pressure of 0.3 Pa in two gas mixtures: (1) Ar and (2) Ar : N_2 = 1 : 1. The collector was located on a satellite rotating orbitally, at a height of 33 cm from the bottom wall of the vacuum chamber.

Table 1. Results for the deposition rate of each component of the high-entropy alloy

	TiAl	Mo	Nb	Cr
I_d, A	130	150	100	150
V_{dep}, μm/h	2.4	1.6	0.8	1.6

The studies of the azimuthal distribution of the ion-current density during the joint operation of five plasma generators (Fig. 3) showed that the uniformity of the ion-current-density distribution varies within 20%, the ion-current density varies from 5.3 to 9.4 mA/cm^2 in argon and from 6.3 to 10 mA/cm^2 in an Ar : N_2 = 1 : 1 gas mixture. In both cases, the minimum is observed for the arc evaporator with an AlTi cathode located on the upper wall of the chamber, and the maximum is observed for the PINK-P gas-plasma generator.

Investigations of the elemental and phase composition and the state of the imperfect substructure were carried out by SEM (Philips SEM-515 instrument with an EDAX ECON IV microanalyzer) and TEM (JEM 2100F instrument, JEOL; equipment of the Central Collective Use Center of the Department of Nanomaterials and Nanotechnologies, Tomsk Polytechnic University). Foils for the TEM measurements were prepared by the ion thinning of plates (an Ion Slicer EM-091001S setup; thinning is carried out with argon ions) cut from bulk samples using an Isomet Low Speed Saw setup perpendicular to the modified surface. This approach made it possible to trace the change in the structure and phase composition of the material at a distance from the sample surface.

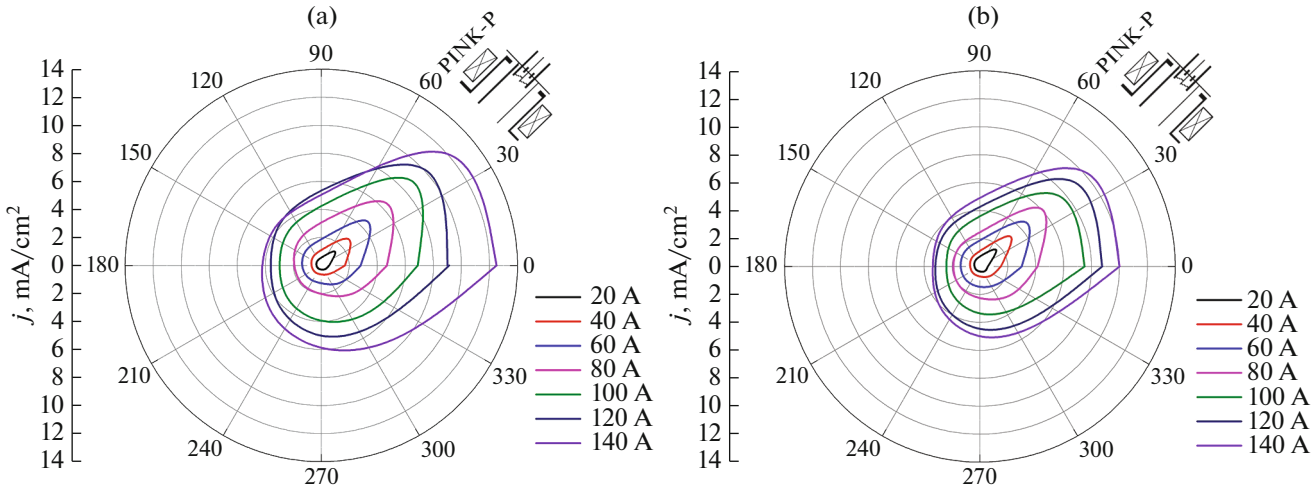

Fig. 2. Azimuthal distribution of the ion-current density j of the gas-plasma generator using (a) pure argon and (b) an Ar : N_2 = 1 : 1 mixture.

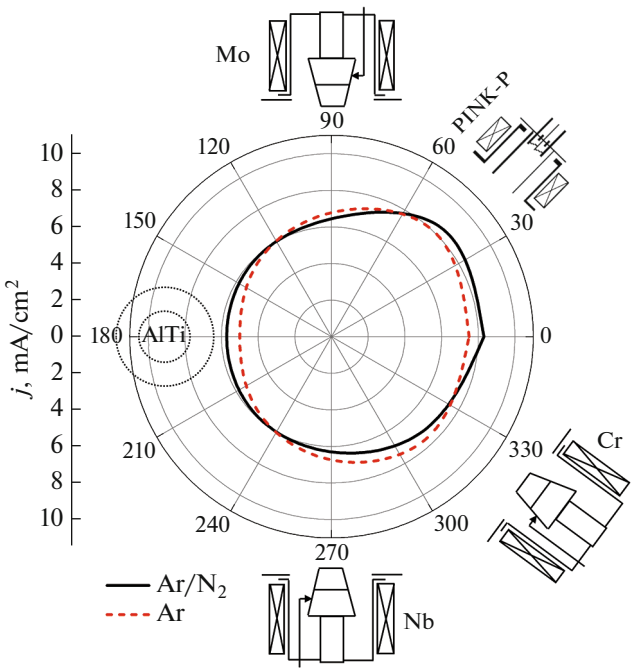

Fig. 3. Azimuthal distribution of the ion-current density j upon the joint operation of all plasma generators.

The phase composition and structural parameters of the samples were studied by XRD using an XRD-6000 diffractometer (CuK_α radiation). The phase composition was analyzed using PDF4+ databases, as well as the POWDER CELL 2.4 full-profile analysis program. The hardness of the films was determined using a PMT-3 device (Vickers method at an indenter load of 0.5 N). Tribological studies of the films were carried out using a Pin on Disc and Oscillating TRIBOtester tribometer (TRIBOtechnic, France) with the following parameters: a ball (counterbody) made of VK8 hard alloy with a diameter of 6 mm, a wear track radius of 2 mm, an indenter load of 2 N, a track length of 50 m, and a sample rotation speed of 25 mm/s. The wear rate of the material was determined from the results of the profilometry of the track formed during the tests. The structure and heat resistance of the films were analyzed using synchrotron radiation. The SR source was the VEPP-3 electron storage ring (Budker Institute of Nuclear Physics, Siberian Branch, Russian Academy of Sciences). We also used an Anton Paar HTK-2000 high-temperature X-ray camera and an OD-3M-350 position-sensitive single-coordinate detector.

RESULTS AND DISCUSSION

The surface structure of the deposited films was studied by the SEM method. Regardless of the deposition mode, particles of the droplet fraction were observed on the surface of the films (Fig. 4). The particle sizes vary within ~0.1–1 μm.

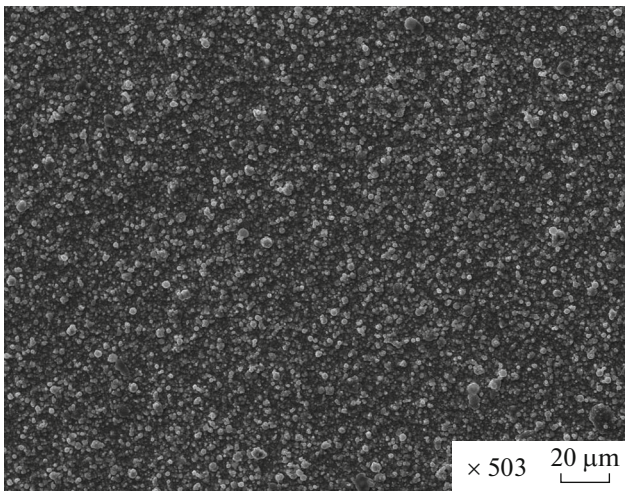

Fig. 4. SEM image of a cermet film of the high-entropy alloy NbMoCrTiAl–N deposited onto a VT1-0 substrate.

Studies of the phase composition of the cermet high-entropy-alloy films on the VK8 hard-alloy substrate proved that the films are X-ray amorphous material. The diffraction pattern (Fig. 5) reveals a wide maximum and a relatively large number of narrow diffraction maxima corresponding to tungsten carbide (substrate).

Assuming the intermetallic phases of the chemical composition of the high-entropy alloy in the deposited film, the revealed diffraction maximum can be represented as a superposition of the diffraction maxima of the following phases: $Ti_{1.08}Mo_{0.4}Al_{0.52}$ (a = 0.31869 nm), $Nb_{0.2}Cr_{0.2}Mo_{0.6}$ (a = 0.31098 nm), and $Ti_{0.66}Nb_{0.07}Mo_{0.27}$ (a = 0.32389 nm). With a relative ratio of these phases of 0.05 : 0.7 : 0.25, the average value of the crystal-lattice parameter of the alloy is

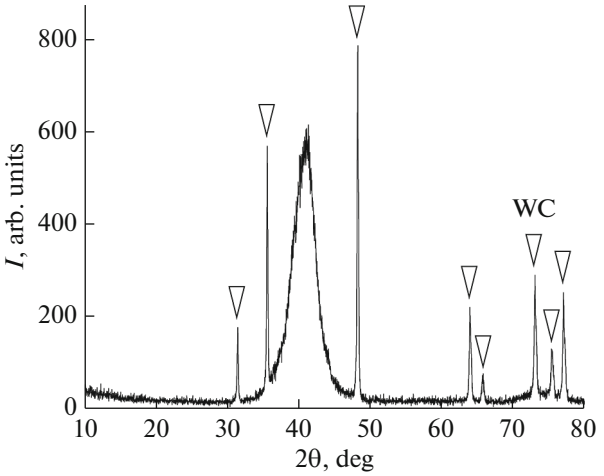

Fig. 5. Part of the diffraction pattern of a cermet film of a high-entropy NbMoCrTiAl–N alloy deposited on VK8 hard alloy.

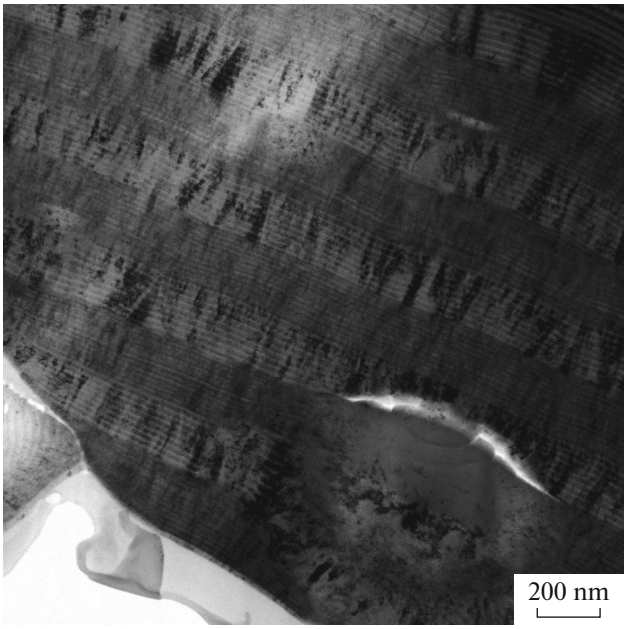

Fig. 6. TEM image of a cermet film of a high-entropy NbMoCrTiAl–N alloy deposited onto a VT1-0 substrate.

0.31459 nm, and the crystal lattice type is body-centered cubic (bcc). The size of the coherent-scattering regions of the alloy is 9.7 nm, which indicates that the film is nanocrystalline. We note that the diffraction maxima of most nitrides formed from chemical elements of a high-entropy alloy fall within this angular range.

The TEM results suggest that the cermet films of high-entropy alloy are a multilayer material (Fig. 6). Visually, the layers differ in contrast; i.e., there are layers of dark and light contrast. The multilayer nature of the films is revealed at two scale levels: microscale level and nanoscale level. At the microscale level, the thickness of the dark contrast layers is 0.21 μm, and that of the light contrast layer is 0.19 μm. Each layer has a layered nanoscale substructure. The substructure thickness of the dark layers is ≈20 nm, and that of the light layers is ≈12 nm. The number of sublayers in the microscale dark layers is ≈10; and in the microscale light layers, it is ≈15.

X-ray spectral microanalysis revealed the separation of the alloy according to the elemental composition (Fig. 7). At the microscale level, layers enriched in nitrogen (Fig. 7d), chromium (Fig. 7e), and aluminum (Fig. 7f) are distinguished. Titanium atoms tend

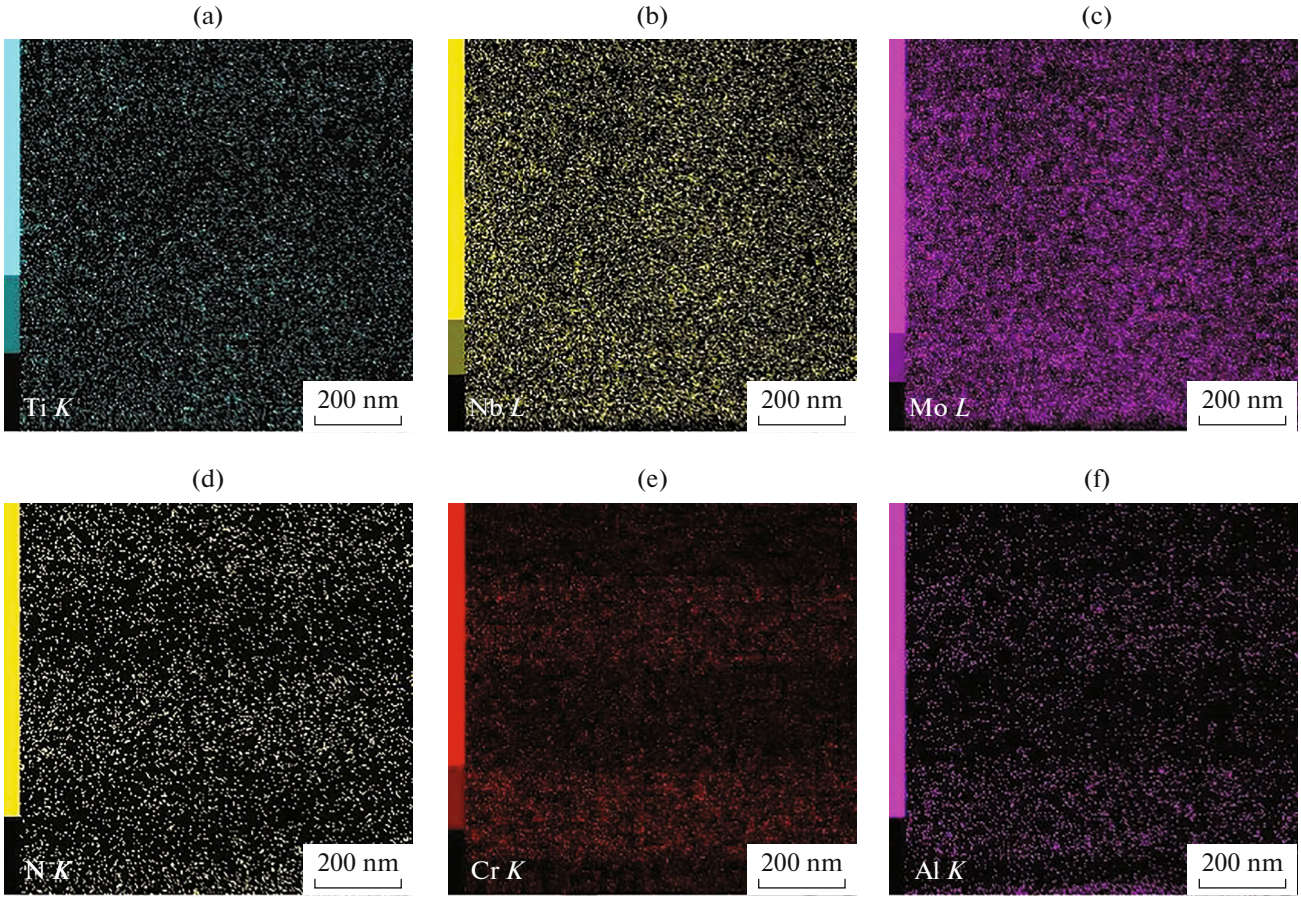

Fig. 7. Distribution maps of (a) Ti, (b) Nb, (c) Mo, (d) N, (e) Cr, and (f) Al atoms in a cermet film of the high-entropy alloy NbMoCrTiAl–N deposited on a VT1-0 substrate.

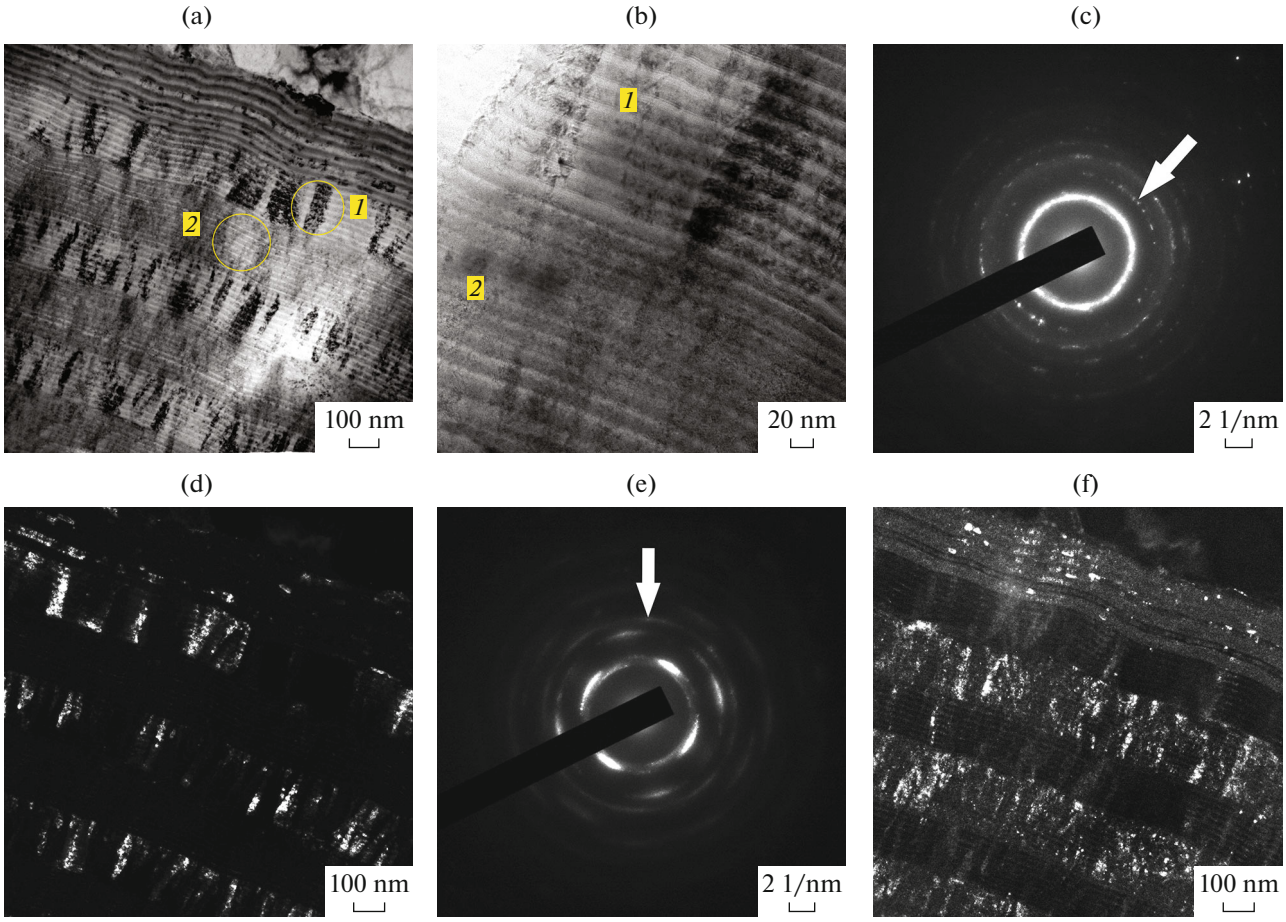

Fig. 8. TEM image of a high-entropy-alloy NbMoCrTiAl–N film deposited on VT1-0 samples: (a, b) bright-field; (c, e) electron-diffraction patterns of segments *1* and *2*, respectively; (d, f) dark-field images obtained using reflections (d) 200 MoNbCrTiAl + 220 TiN and (f) 211 MoNbCrTiAl + 004 TiN + 200 MoN + 200 NbN. The arrows indicate the reflections used to obtain dark-field images.

toward layers enriched in nitrogen (Fig. 7a). The layers enriched in nitrogen are depleted in chromium and aluminum atoms. At the nanoscale level, layers enriched in aluminum and layers enriched in chromium, molybdenum, and niobium are detected.

The result of dark-field analysis shows that the revealed layers have a nanocrystalline columnar structure with a crystallite size varying within 5–10 nm (Fig. 8). The electron-diffraction patterns (Figs. 8c and 8e) indicate a material with a bcc crystal lattice based on the totality of interplanar distances. This result is in good agreement with the XRD data (Fig. 5). The electron-diffraction patterns corresponding to dark and light microscale layers show broad blurred diffraction rings, which indicates, first, the nanocrystalline structure of the film, second, the presence of an amorphous component in the film, and, third, the presence of phases of variable composition. The indexing of the electron-diffraction patterns shows that the microscale layers with a light contrast (layers *1* in Figs. 8a and 8b) correspond to the MoNbCrTiAl–N solid solution. A blurred first diffraction ring in the electron-diffraction pattern (Fig. 8c) may indicate crystallites of other phases in these layers, for example, nitrides. Microscale layers with a dark contrast (layers *2* in Figs. 8a and 8b), which correspond to the electron-diffraction pattern characteristic of amorphous-crystalline phases (Fig. 8e), can be formed by nitrides of chemical elements present in the high-entropy alloy.

XRD using SR studies of multilayer cermet coatings of a high-entropy alloy based on Ti, Al, Cr, Mo, Nb, and N for heat resistance showed that the coatings have a structure close to that of molybdenum. When heated in air, the decomposition of the system begins at a temperature of 630–640°C (Fig. 9). At 1070–1080°C, new reflections appear, presumably related to oxide compounds of the alloy components. The reflections of the high-entropy alloy completely disappear at temperatures of 1260–1270°C. Further, as the coating begins to collapse, it is impossible to determine the final state.

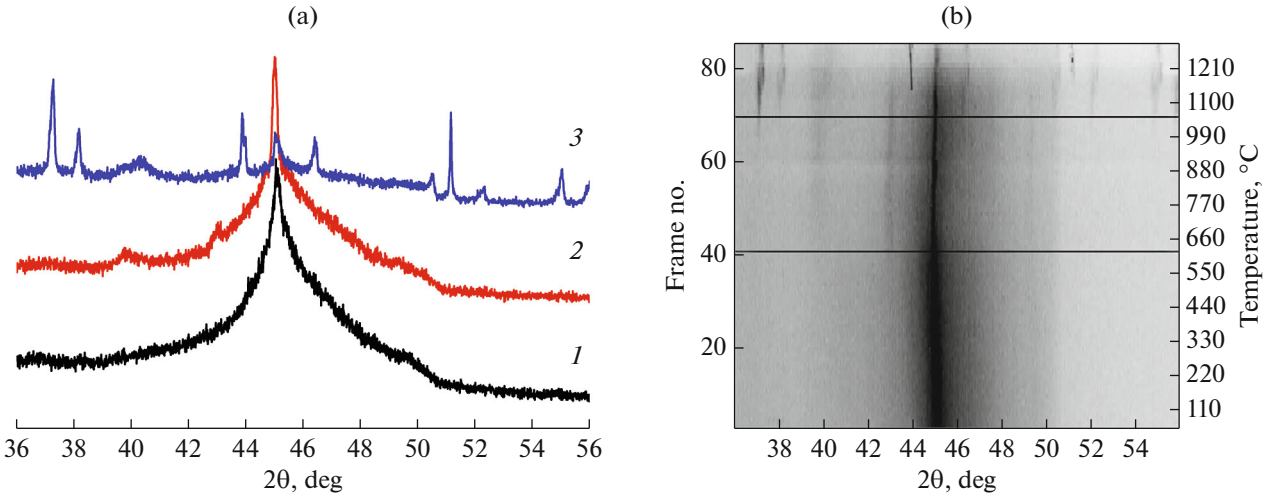

Fig. 9. (a) X-ray diffraction patterns of the AlTiCrNbMo–N film obtained at (*1*) 50, (*2*) 900, and (*3*) 1300°C ($\lambda = 0.172$ nm). (b) A complete set of diffraction patterns during heating from room temperature to 1300°C. The film was deposited onto tungsten samples.

Thus, the SR results prove that the cermet coatings of the high-entropy alloy AlTiCrNbMo–N are stable when heated in air to temperatures not exceeding 620°C.

The microhardness measurements of the cermet film of high-entropy alloy deposited on a VK8 hard-alloy substrate, performed at an indenter load of 0.5 N, yielded a microhardness of 27.0 GPa and Young's modulus of 176 GPa.

The wear parameter (the value inversely proportional to the wear resistance) of the cermet film of the alloy deposited on the VK8 hard-alloy substrate is 6.4×10^{-6} mm^3/N m, and its friction coefficient is 0.20.

CONCLUSIONS

We studied the rate of deposition of individual components of the coatings and the parameters of the generated plasma with the independent and joint operation of plasma sources. The azimuthal distribution of the ion-current density of the gas-plasma generator was also investigated during the joint operation of four metal plasma generators. The uniformity of the ion-current-density distribution varies within 20%.

The formed cermet films of a high-entropy alloy have a nanocrystalline layered structure with a crystallite size of 5–10 nm. The microhardness of the films depends on the concentration of chemical elements and reaches 27 GPa. The wear parameter of 6.4×10^{-6} mm^3/N m and the friction coefficient of 0.2 for cermet films weakly depend on the deposition mode.

The XRD and SR results for the heat resistance of multilayer cermet coatings of a high-entropy alloy show that the coatings have a structure close to that of molybdenum. When heated in air, decomposition of the system begins at a temperature of 630–640°C. At 1070–1080°C, new reflections appear, presumably related to oxide compounds of the alloy components. The reflections of the high-entropy alloy completely disappear at temperatures of 1260–1270°C.

FUNDING

The work was supported by the Ministry of Science and Higher Education of the Russian Federation (project no. 075-15-2021-1348) within the framework of activities no. 2.1.5, 2.1.17, and 2.1.20.

CONFLICT OF INTEREST

The authors declare that they have no conflicts of interest.

REFERENCES

1. B. Cantor, I. T. H. Chang, P. Knight, and A. J. B. Vincent, Mater. Sci. Eng., A **375**, 213 (2004). https://doi.org/10.1016/j.msea.2003.10.257
2. J.-W. Yeh, S.-K. Chen, S.-J. Lin, J.-Y. Gan, T.-S. Chin, T.-T. Shun, C.-H. Tsau, and S.-Y. Chang, Adv. Eng. Mater. **6**, 299 (2004). https://doi.org/10.1002/adem.200300567
3. S. Ranganathan, Curr. Sci. **85**, 1404 (2003).
4. A. D. Pogrebnjak, A. A. Bagdasaryan, I. V. Yakushchenko, and V. M. Beresnev, Russ. Chem. Rev. **83**, 1027 (2014). https://doi.org/10.1070/RCR4407
5. D. B. Miracle and O. N. Senkov, Acta Mater. **122**, 448 (2017). https://doi.org/10.1016/j.actamat.2016.08.081
6. S. Praveen and H. S. Kim, Adv. Eng. Mater. **20**, 1 (2018). https://doi.org/10.1002/adem.201700645
7. E. J. Pickering and N. G. Jones, Int. Mater. Rev. **61**, 183 (2016). https://doi.org/10.1080/09506608.2016.1180020

8. Ch.-H. Lai, S.-J. Lin, L.-W. Yen, and Sh.-Y. Chang, Surf. Coat. Technol. **201**, 3275 (2006). https://doi.org/10.3103/S106345761802003X
9. A. S. Rogachev, Phys. Met. Metallogr. **121**, 733 (2020). https://doi.org/10.1134/S0031918X20080098
10. O. V. Sobol', A. A. Andreev, V. F. Gorban', N. A. Krapivka, V. A. Stolbovoi, I. V. Serdyuk, and V. E. Fil'chikov, Tech. Phys. Lett. **38**, 616 (2012).
11. H. Chen, A. Kauffmann, B. Gorr, D. Schliephake, C. Seemuller, J. N. Wagner, H. J. Christ, and M. Heilmaier, J. Alloys Compd. **661**, 206 (2016). https://doi.org/10.1016/j.jallcom.2015.11.050
12. O. N. Senkov, G. B. Wilks, J. M. Scott, and D. B. Miracle, Intermetallics **19**, 698 (2011). https://doi.org/10.1016/j.intermet.2011.01.004
13. O. N. Senkov, J. M. Scott, S. V. Senkova, D. B. Miracle, and C. F. Woodward, J. Alloys Compd. **509**, 6043 (2011). https://doi.org/10.1016/j.jallcom.2011.02.171
14. N. N. Guo, L. Wang, L. S. Luo, X. Z. Li, Y. Q. Su, J. J. Guo, and H. Z. Fu, Mater. Des. **81**, 87 (2015). https://doi.org/10.1016/j.matdes.2015.05.019
15. O. N. Senkov, S. V. Senkova, D. B. Miracle, and C. Woodward, Mater. Sci. Eng., A **565**, 51 (2013). https://doi.org/10.1016/j.msea.2012.12.018
16. N. N. Trofimenko, I. Yu. Efimochkin, and A. N. Bol'shakova, Aviats. Mater. Tekhnol., No. 2, **3** (2018). https://doi.org/10.18577/2071-9140-2018-0-2-3-8
17. C. C. Juan, M. H. Tsai, C. W. Tsai, et al., Intermetallics **62**, 76 (2015). https://doi.org/10.1016/j.intermet.2015.03.013
18. B. Schuh, F. Mendez-Martin, B. Volker, E. P. George, H. Clemens, R. Pippan, and A. Hohenwarter, Acta Mater. **96**, 258 (2015). https://doi.org/10.1016/j.actamat.2015.06.025
19. G. V. Fetisov, *Synchrotron Radiation: Methods for Studying the Structure of Substances*, Ed. by L. A. Aslanov (Fizmatlit, Moscow, 2007) [in Russian].
20. Yu. F. Ivanov, N. N. Koval, O. V. Krysina, T. Baumbach, S. Doyle, T. Slobodsky, N. A. Timchenko, R. M. Galimov, and A. N. Shmakov, Surf. Coat. Technol. **207**, 430 (2012). https://doi.org/10.1016/j.surfcoat.2012.07.037
21. O. V. Krysina, N. N. Koval, A. N. Shmakov, and Z. S. Vinokurov, J. Phys.: Conf. Ser. **669**, 12034 (2016). https://doi.org/10.1088/1742-6596/669/1/012034
22. N. A. Timchenko, Ya. V. Zubavichus, O. V. Krysina, S. I. Kuznetsov, M. S. Syrtanov, and S. V. Bondarenko, J. Surf. Invest.: X-ray, Synchrotron Neutron Tech. **10**, 425 (2016). https://doi.org/10.1134/S1027451016020373
23. O. V. Krysina, N. N. Koval, S. S. Kovalsky, V. V. Shugurov, I. V. Lopatin, N. A. Prokopenko, and E. A. Petrikova, Vacuum **187**, 110123 (2021). https://doi.org/10.1016/j.vacuum.2021.110123
24. Yu. F. Ivanov, N. N. Koval, Yu. H. Akhmadeev, V. V. Uglov, V. V. Shugurov, E. A. Petrikova, O. V. Krysina, N. A. Prokopenko, and I. I. Azhazha, Russ. Phys. J. **64**, 2207 (2022). https://doi.org/10.1007/s11182-022-02578-5

Translated by O. Zhukova